JOURNAL OF AIRCRAFT
Vol. 50, No. 1, January–February 2013

Numerical Investigations of Lateral Characteristics of an Air-to-Air Missile

R. Balasubramanian,* Vaibhav Shah,† Konark Arora,† R. Krishnamurthy,‡ and Debasis Chakraborty§
Defence Research and Development Laboratory, Hyderabad 500058, India

DOI: 10.2514/1.C031761

Numerical simulations were carried out for investigating the lateral aerodynamic characteristics of an air-to-air missile using an in-house-developed Reynolds-averaged Navier–Stokes code, CERANS. The analyses were carried out for Mach numbers from 0.8 to 2.0 and angles of attack ranging from 10 to 20 deg for roll sweeps from −45 to +90 deg. The rolling-moment behavior of the missile at Mach 1.2 and an angle of attack of 15 deg was explicitly and exhaustively analyzed because this flight condition is critical from the point of view of severe induced roll. The necessity of studying the rolling-moment behavior at finer roll orientations is demonstrated. The main objectives of the investigations are to explain the governing physical phenomenon and the resultant complex flow behavior that caused excessive induced roll generated during the critical flight condition.

I. Introduction

AN AIR-to-air missile (AAM) reaches a critical phase of flight when the Mach number of the flight is 1.2 to 1.5, the effective angle of attack is around 11 to 15 deg, and the altitude of flight is about 2 to 2.5 km. During this phase, the missile experiences severe rolling moment, and it has been conjectured that the complex aerodynamic interactions encountered during flight could be the cause of this excessive rolling of the missile. Hence, a detailed investigation of the aerodynamic flowfield during this critical phase of flight was carried out to bring out the cause of the severe missile roll. Also, the study should further assist with design modifications to the airframe, leading to the alleviation of the excessive roll. The only viable option of investigation in the stringent time-bound missile design cycle is to perform numerical simulations, because any wind-tunnel-based study will be time-consuming. Hence, the in-house-developed Computational Fluid Dynamics (CFD) code CERANS© [1] was used for simulating and analyzing the critical flight conditions.

II. Grid Generation

The AAM airframe configuration is shown in Fig. 1. The geometry consists of an ogive-nose with cruciform low-aspect ratio wings, cruciform fins in-line with the wings, a pair of diagonally opposite wire-tunnels, and three launch shoes at various locations. In the present study, launch shoes were not considered in the geometry modeling.

The computational grid was generated using the in-house-developed codes DRDL-SUMO and AUTOELGRID© [2]. A surface model of the AAM with wings, fins, and wire-tunnels was developed using SUMO. Around this surface model, structured hexahedral volume grids with four blocks were generated using AUTOELGRID. Further the grid was enriched with boundary layer mesh, generated using a separate extrusion grid generator, thereby enabling us to perform viscous computations. For various test cases, grid sizes varying from about 4.7 to about 11 million elements were generated. A typical grid in the pitch plane is shown in Fig. 2. For the present study, a grid size of about 4.7 million elements was chosen based on a grid independence study made with 1.0, 4.7, and 7.8 million-element grids. The difference in aerodynamic coefficients between the 4.7 and 7.8 million-element grids was found to be less than 3%, and hence, the grid containing 4.7 million elements was chosen for the production runs carried out in this study.

III. CERANS© Flowsolver and Computational Details

The in-house-developed Message Passing Interface (MPI) parallel implicit RANS flowsolver CERANS© [1] was used for all the flow simulations. The interfacial numerical fluxes for the mean flow equations were evaluated using modified Roe's flux formulae for the convective fluxes and central differencing for the diffusive fluxes. Second-order spatial accuracy was used for evaluating the mean flow fluxes and a slope limiter was used to preserve monotonicity in regions of discontinuities. The one-equation Spalart–Allmaras turbulence model was used for addressing the closure problem. A local time step was used for time evolution. Convergence was accelerated with a point Jacobi-based implicit procedure and the criteria used for convergence was based on an asymptotic steady-state limit of the aerodynamic coefficients. In the present study, the computations were carried out using the 128-core HYPERCOM and 56-core MINICRUNCH systems of DRDL. Overall, about 250 simulations were carried for the entire investigation.

IV. Results and Discussion

Because the missile was undergoing rolling motion during the critical phase of the flight as a result of complex flow interactions over the geometry, simulations were required to be performed for various "roll orientations." The geometric details of the roll angles are provided in Fig. 3. In the present study, the missile was pre-rotated by angle "ϕ," called the "angle of roll" with respect to the "zero" degree configuration shown in Fig. 3, and steady-state simulations were carried out for each of the roll angles considered. In actuality, the overwhelming lateral loads generated during flight, if any, should have caused the missile to roll against the missile lateral inertia, with a time lag for such lateral forces to act on the airframe. However, if the missile was to stay rigid, resisting any roll (infinite inertia), then the lateral forces due to the lateral aerodynamic loads should be much higher than if the missile were allowed to roll. Hence, the loads that were estimated at such a steady-state should be higher, and hence, the lateral load estimates presented here shall be considered conservative.

Presented at the Symposium on Applied Aerodynamics and Design of Aerospace Vehicle (SAROD-2011), Bangalore, India, 16–18 November 2011; received 25 November 2011; revision received 16 March 2012; accepted for publication 23 May 2012; published online 4 December 2012.

*Scientist, CFD Division. E-mail: bals.cfd@gmail.com (Corresponding Author).
†Scientist, CFD Division.
‡Head, CFD Division.
§Technology Director, Computational Dynamics.

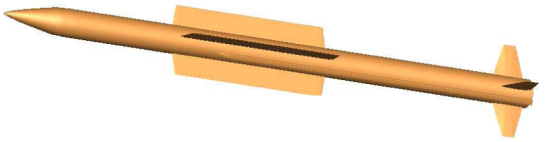

Fig. 1 AAM configuration.

The comprehensive aerodynamic database based on the wind-tunnel study had provided aerodynamic parameters for several roll angles from 0 to 180 deg in discrete roll orientations. In the present study, simulations were carried out in finer intervals of roll position to estimate the roll characteristics of the missile.

A. Comparison of Longitudinal Characteristics

Although the aim of the present investigation is evaluation of lateral characteristics and explaining the cause of severe roll during the critical flight phase of the AAM, for the sake of assessment of the accuracy of the CERANS code, the longitudinal characteristics were compared with the wind-tunnel data for the available roll orientations. Typical plots of Mach number contours for freestream conditions of Mach 1.2, angle of attack of 15 deg, and roll angle of 57 deg in pitch plane depicting the nose, wing, and fin shock is presented in Fig. 4.

The total pressure-loss contours and isopressure contours at a wing cross section location are presented in Fig. 5. The flow roll-up over the wing depicting low-pressure cores can be clearly observed from the pictures. The crossflow vortices from the wings and wire-tunnels and the asymmetric nature of the vortex pattern can be clearly observed. Similarly, the total pressure-loss contours and isopressure contours for the fin cross section are shown in Fig. 6. The figures depict the envelope shock and the additional complex pressure field around the fins. The total pressure-loss contours shown in Fig. 6 clearly depict the highly complex and asymmetric nature of the flowfield.

From Figs. 7 and 8, it can be observed that the comparison of normalized coefficients of normal (C_N) and side force (C_S) between CERANS and the wind-tunnel data for various roll angles at Mach 1.2 and angle of attack of 15 deg is very good.

B. Variation of Coefficient of Rolling Moment with Angle of Roll

Initially, for the roll angle range from -45 to $+90$ deg for Mach 1.2 and $\alpha = 15$ deg, simulations were carried out for roll angles only in steps of 22.5 deg, as was carried out in wind-tunnel experiments, so that a comparison between the CFD prediction and wind-tunnel data can be made. The plot depicting the variation of normalized coefficient of rolling moment (C_l or CRM) with roll angles in steps of 22.5 deg is shown in Fig. 9. The null-rolling moment after normalization is 2.8. It can be observed that the trends of the CFD and wind-tunnel data are similar; however, the magnitudes of the wind-tunnel values are smaller than those of the CFD data. At 45-deg roll, both CFD and the wind-tunnel data should predict a zero CRM value because the geometry is perfectly symmetric in the α-plane. In this case, the CFD-predicted CRM is exactly zero, whereas the wind-tunnel data show a small non-zero CRM value. Although the predicted trends of both methods are the same, the slope $dC_l/d\phi$ of the CFD data is twice that of the wind-tunnel data in the roll angle range of 0 to 90 deg.

Further, simulations were carried out for Mach 2.0 and an angle of attack of 20 deg and the results are presented in Fig. 10. It is very interesting to note that the agreement between the wind-tunnel data and the CFD data is good.

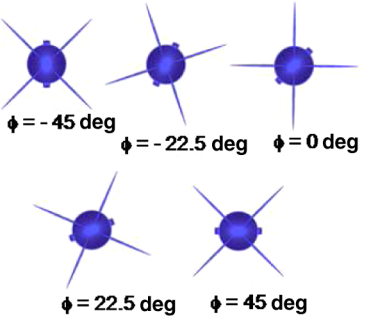

Fig. 3 Definition of roll angles (rear view).

C. Roll Characteristics at Finer Angle of Roll Intervals

During the critical phase of flight when the missile roll started to build up, its roll orientation was no longer that of the launch roll angle of 45 deg; instead, it had been rotating at about one revolution per second. For roll angles lying within the 22.5 deg interval, there are no data available in the aerodynamic database. Hence, simulations were made at finer angle of roll intervals until the CRM vs ϕ curve was built up. The enriched plot depicting the variation of normalized CRM with finer roll angle intervals is shown in Fig. 11. There are significant differences between the predicted CRM and experimental CRM. But at a discrete point when the experimental data are available, the agreement between the CFD and experiment is very good. However, the experimental data failed to capture the true rolling moment characteristics.

This entire exercise had unraveled a CRM vs ϕ behavior that was entirely different from that of the higher roll-angle step-based analysis. For roll angles from -45 to -15 deg, a sine-wave-like variation can be observed. In this region, where the 22.5 deg step analysis showed a lower slope, the finer step analysis revealed two sign changes in slope and, importantly, a peak CRM value of about 3.8, whereas the previous analysis had shown no peaks. The slope of the CRM variation in the region of about -28 to -18 deg roll angle is very large. Similarly, for roll angles from 22.5 to 67.5 deg, the variation is significantly different, with a large slope and two sign changes in slope.

The preceding analysis had thrown new light into the way roll behavior needs to be modeled and inducted into the system analysis.

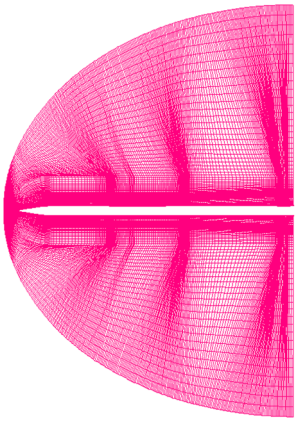

Fig. 2 Grid in pitch plane.

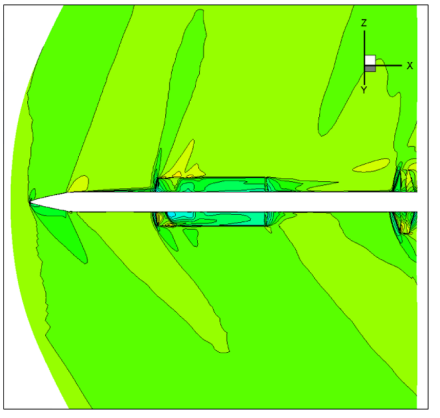

Fig. 4 Mach contours in pitch plane.

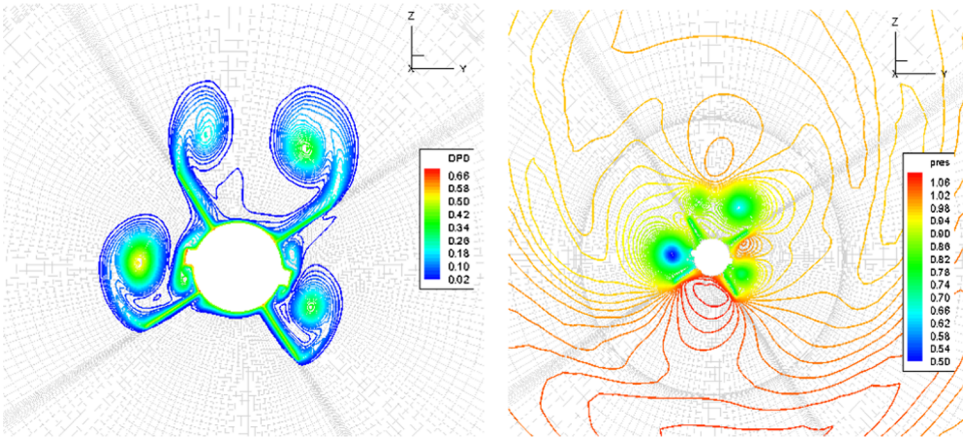

Fig. 5 Pressure-loss and isopressure contours at wing cross section.

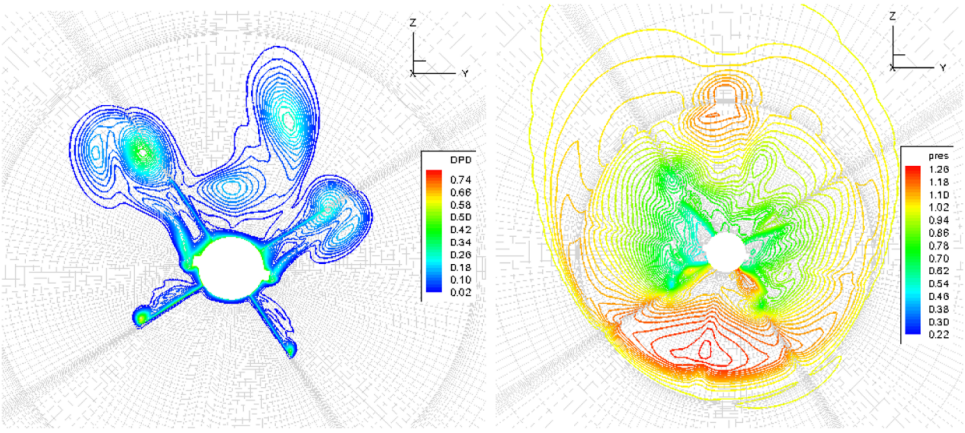

Fig. 6 Pressure-loss and isopressure contours at fin cross section.

A major conclusion that can be drawn from this exercise is that a 22.5 deg step interval for roll angle does not represent in any way the true roll behavior of the missile. In fact, it grossly fails to spot the occurrence of important crests and troughs. Thus, for thorough analysis of the roll behavior of missiles, it is necessary to consider finer intervals of roll angle during the roll sweep, be it through wind-tunnel experiments or numerical simulation.

D. Typical Case Study at Angle of Roll of −34 deg

The CRM for this case, as can be observed from Fig. 11, is about 3.8, with a positive peak value in the range of $-45 \text{ deg} \leq \phi \leq 45 \text{ deg}$. It is hence considered for detailed examination. The angle of attack of 15 deg shall be considered as a "moderately high angle of attack" due to the geometry having surfaces like wings and fins and the flow patterns were observed to be quite complex. If the geometry is just a body of revolution and does not have any surfaces, then the flow pattern over the geometry is uncomplicated and such angles of attack shall be described as low to moderate.

Normalized total pressure contours or total pressure-loss contours typically represent vorticity in the flowfield as per Crocco's theorem of gas dynamics, which states that the vorticity is proportional to the entropy gradient, which in turn can be represented by the ratio of total pressure to the freestream stagnation pressure. Hence, the total pressure-loss contours are the ideal choice for depicting vorticity in the flowfield and have been used to represent the vortical flowfield in this paper.

For $\phi = -34$ deg, the vortical flow patterns at various cross-sectional planes along the axial direction of the missile are shown from Figs. 12 to 23. It is observed that from the nose up to about $X = 3.4D$, the near-body flowfield is completely dominated by the

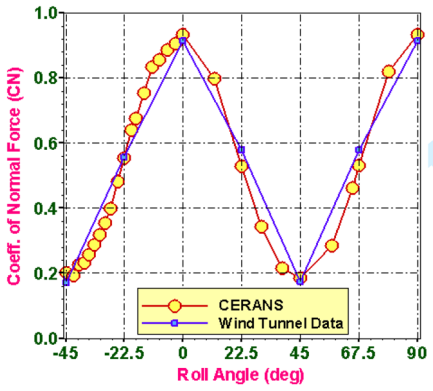

Fig. 7 Variation of C_N with ϕ.

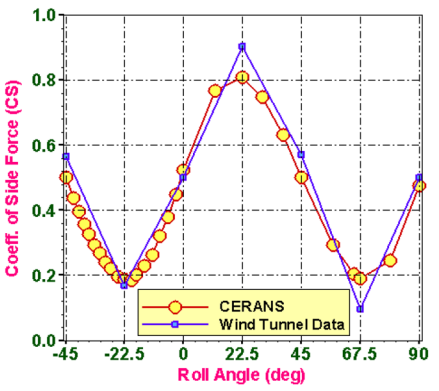

Fig. 8 Variation of C_S with ϕ.

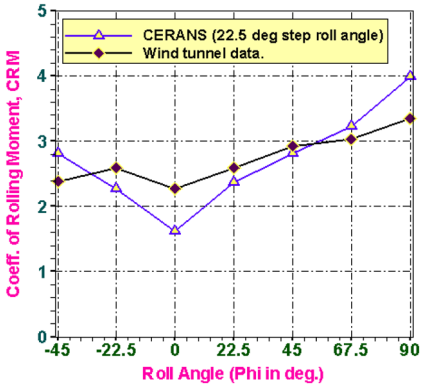

Fig. 9 C_l vs ϕ (22.5 deg step), Mach 1.2, $\alpha = 15$ deg.

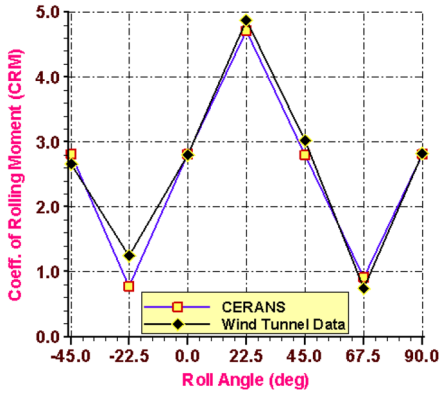

Fig. 10 C_l vs ϕ (22.5 deg step), Mach 2.0, $\alpha = 20$ deg.

axial core flow and the streamlines in the crossflow are fully attached. Aft of this location, the crossflow gains momentum, due to which the streamlines in the leeward side begin to separate. This can be clearly seen from Fig. 12, which is plotted at $X = 4.5D$. Further downstream, at about $5.6D$, the symmetric leeward separation over the missile body gains strength, producing a larger bubble size, as shown in Fig. 13.

At a location of about $7.2D$ from the nose, the wing vortex just starts to form and the leeward side wing delinks the body vortex, which can be clearly seen from Fig. 14. In Fig. 15, at a location of about $8.6D$ from the nose, it can be observed that the body vortex is distorted by the presence of the leeward wings and the vortices lie between the leeward wings. Also, the wing vortex just starts to form, as can be observed at the wing tips. This is also the location at which the wire-tunnels begin. It can be observed that there are about eight visible vortical structures in this cross-sectional plane, viz., four above the wing tips, two smaller body vortices between the leeward and windward wings, and two vortices between the leeward wings,

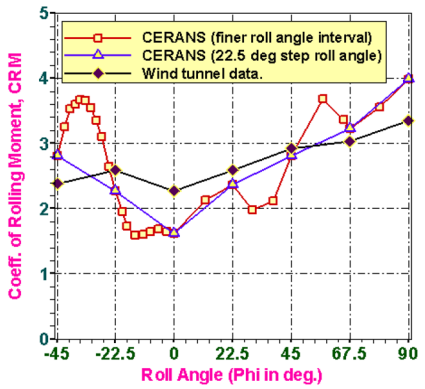

Fig. 11 C_l vs ϕ, Mach 1.2, $\alpha = 15$ deg.

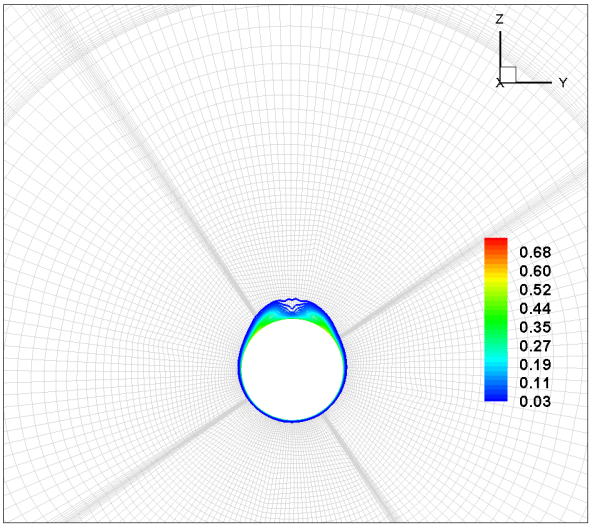

Fig. 12 Crossflow vortices at $X = 4.5D$.

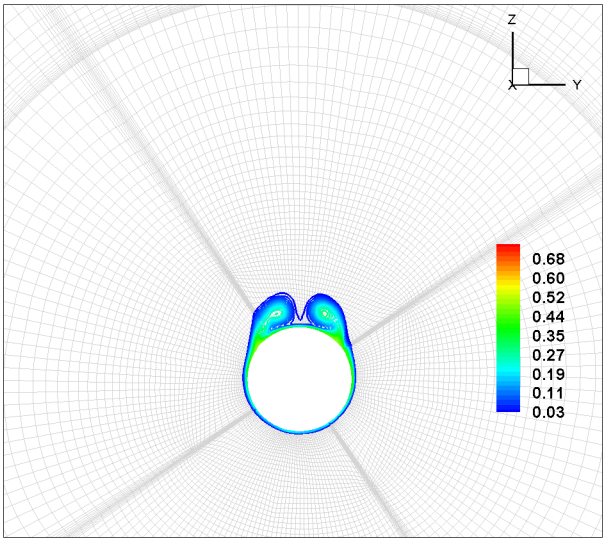

Fig. 13 Crossflow vortices at $X = 5.6D$.

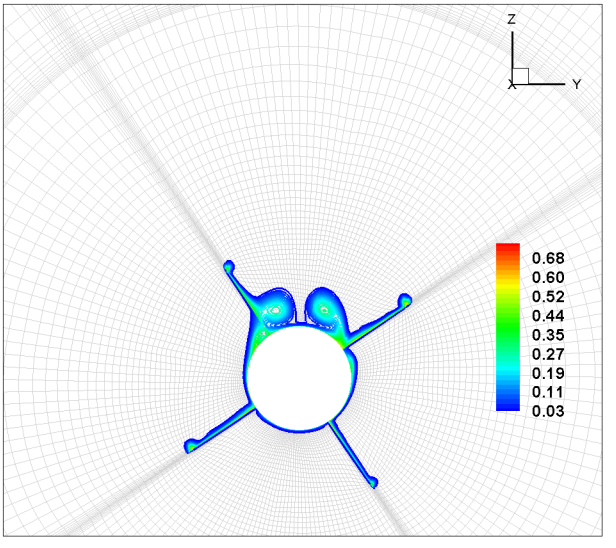

Fig. 14 Crossflow vortices at $X = 7.2D$.

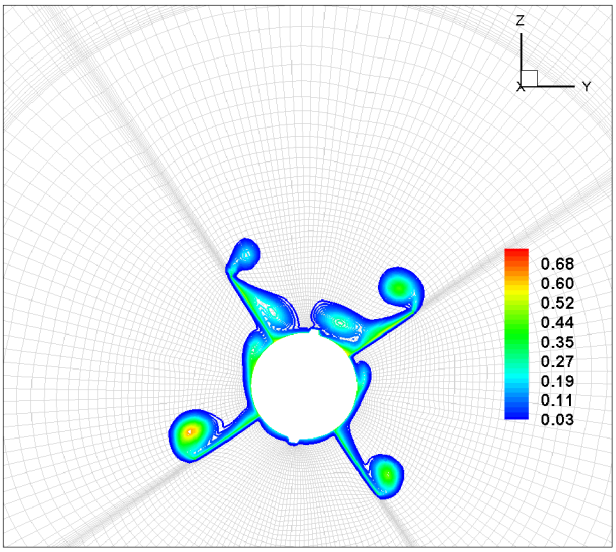

Fig. 15 Crossflow vortices at $X = 8.6D$.

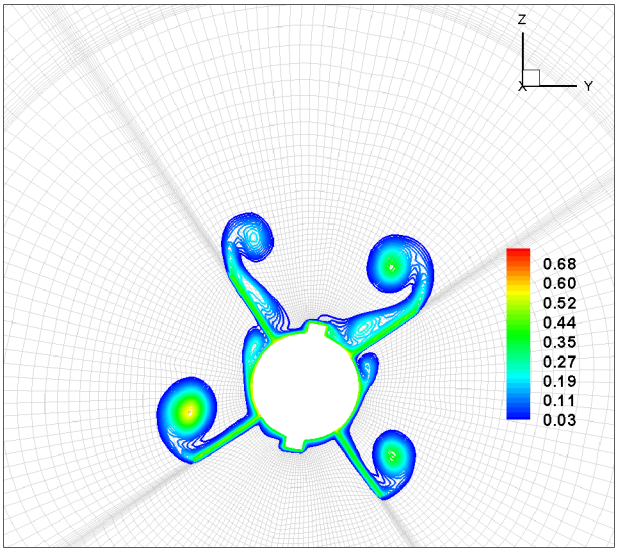

Fig. 16 Crossflow vortices at $X = 10.1D$.

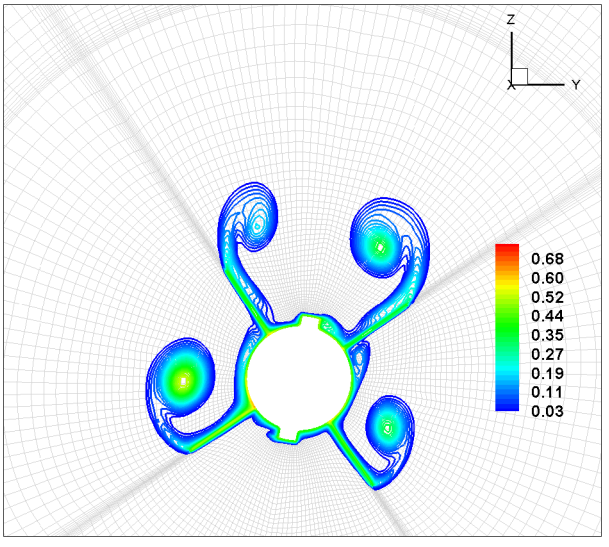

Fig. 17 Crossflow vortices at $X = 11.8D$.

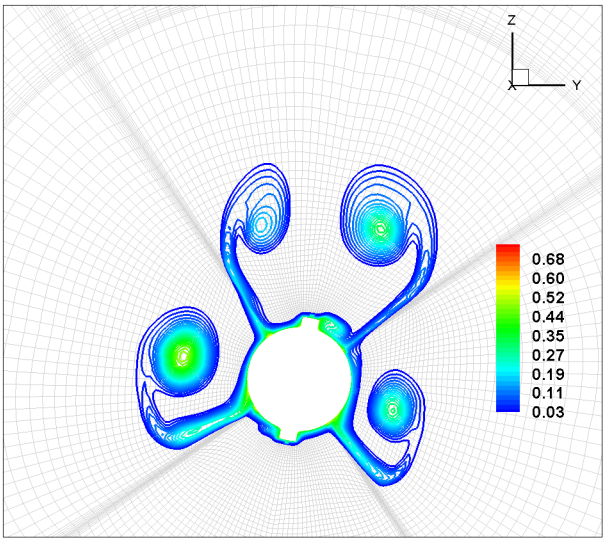

Fig. 18 Crossflow vortices at $X = 14D$.

which are nothing but the body vortices distorted by the leeward wings. From Fig. 16, at $10.1D$, it can be observed that the body vortices sandwiched between the leeward wings are completely drawn inward by the leeward wing-tip vortices. Also adjacent to the leeward side wire-tunnel, a small recirculation zone had formed. From Fig. 17 at $X = 11.8D$, it can be observed that there are no body vortices in the plane and they are completely absorbed by the leeward wing-tip vortices. In fact, the wing-tip vortices had gained their strength partially due to this drawing-in of the body vortices and started to roll up. It can be seen that at the $11.8D$ location, each vortex bubble grew in size considerably as compared to that at the $10.1D$ location.

Also, it can be observed that all the wing-tip vortices have detached from the respective surfaces and started to roll up. From Fig. 18, it can be observed that at $X = 14D$, where the wing ends, the vortices grew in size, becoming completely detached and rolling further upwards. Tracking the vortices further downstream, at $X = 15.2D$, where wire-tunnels are the only protrusion and the wings end, leaving the vortices with no surface to hold on, all the vortices moved quickly upward in the spatial expanse between the wing and fin due to higher momentum in the crossflow, and a couple of them have sizes comparable to the diameter of the missile, as shown in Fig. 19.

At $16.3D$ from the nose, from Fig. 20, it can be noted that the windward wing-tip vortex (on the left side) had rolled up

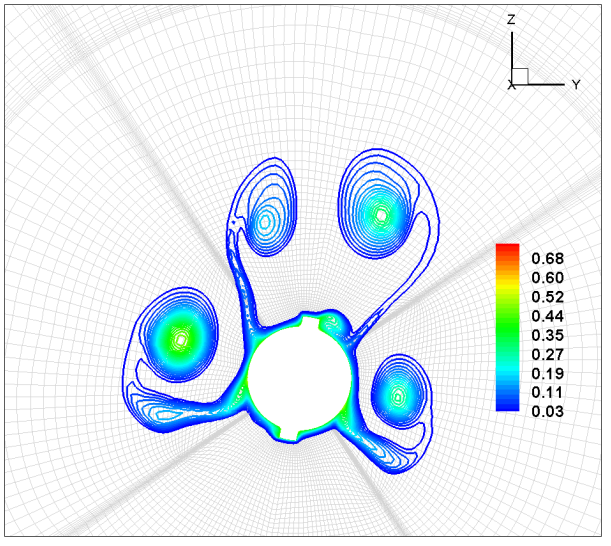

Fig. 19 Crossflow vortices at $X = 15.2D$.

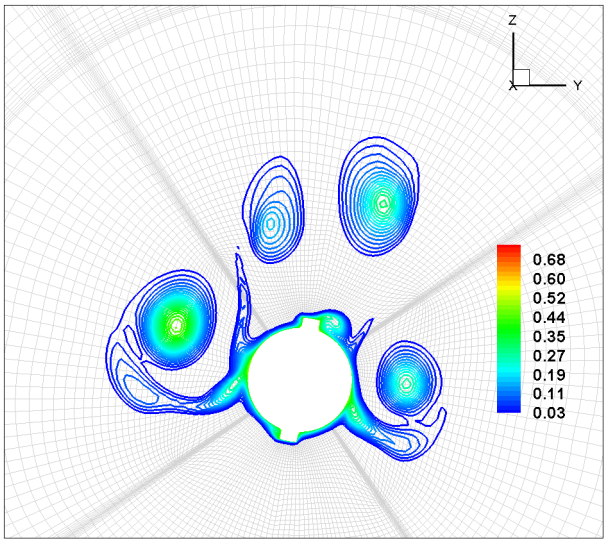

Fig. 20 Crossflow vortices at $X = 16.3D$.

considerably, placing it closer to the leeward wing-plane. Also, the leeward vortices have completely detached and started to distort. As the distortion continues and the roll-up enhances further, the windward wing-tip vortices on both sides started to cross over the leeward wing planes. Also, the detached leeward wing-tip vortices started to move towards the mid-plane between the leeward wings and their shapes were distorted to oval shapes. Although smaller than the body diameter, the two vortices have sizes comparable to the size of the missile body cross section. These features can be observed from Fig. 21.

At a cross section of $19.7D$ from the nose where the fin root leading edge starts, windward wing-tip vortices rolled up to such an extent that they started to strongly interact with the fins. Because the size and hence the strength of the vortex bubble on each side is different, as can be observed from Fig. 22, the vortices impart differential vortex pressure loads on the fins, thereby resulting in severe sideward load and the consequential severe rolling moment. It can be observed that the detached leeward vortex, which had been associated with the left leeward wing, was pushed to move further towards the mid-plane of the lee side.

The flow pattern becomes very complicated with the windward vortex dislodging the leeward vortex on either side, resulting in asymmetric aerodynamic loading on the airframe. Once the windward vortex on the left side reaches the left leeward fin, it in fact

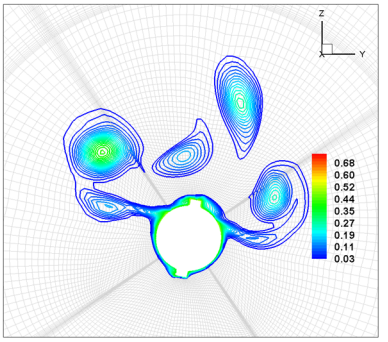

Fig. 22 Crossflow vortices at $X = 19.7D$.

brushes the leeward fin tip firmly. Similarly, on the right side, the relatively smaller vortex impinges on to the right leeward fin. Also the fin-tip vortices started to form, as can be observed for the windward fins, whereas the wing-tip vortices of the leeward fins were completely complicated by the upstream vortical flow. These features can be observed from Fig. 23.

Summarizing, the asymmetric impingement of crossflow wing vortices on the fins adversely affected the lateral characteristics of the missile, leading to the surging of fin loads to large magnitudes. This was true for most of the ϕ orientations except for the symmetric or close to symmetric orientations. In all cases, what had started as a purely symmetric flow pattern at the nose tend to become very complicated by the time it passed over the fins. It is well known from the literature that if the flowfield over an aircraft is vortex-dominated and if the vortices create adverse roll of the aircraft, then such a roll effect is called a "vortex induced roll" or simply "induced roll." Although the preceding description of flow patterns over the missile using discrete cross-sectional vortical flow features is piecemeal in manner, such an analysis actually could convey the hot-beds of complexity as to what could happen in reality under such flow conditions.

E. Cumulative Rolling-Moment Distribution

The normalized cumulative CRM distribution along the axial stations of the missile indicates the magnitude of integrated rolling moment experienced at each axial station. For $\phi = -34$ deg, the plot of the cumulative CRM along the axial direction is shown in Fig. 24. The null-rolling moment value due to normalization is 2.8. It can be observed that the rolling moment is 2.8 all through the body of revolution where symmetry of flow is maintained. At the beginning location of the wing, it can be seen that the wings start contributing to the rolling moment and the value of CRM is about 2.6. Further

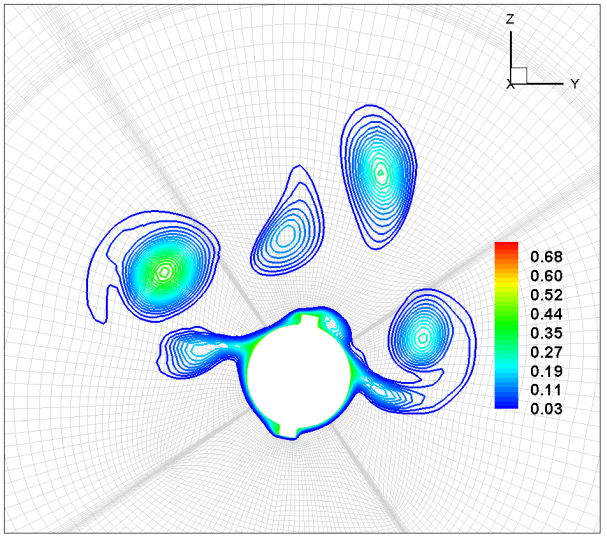

Fig. 21 Crossflow vortices at $X = 18D$.

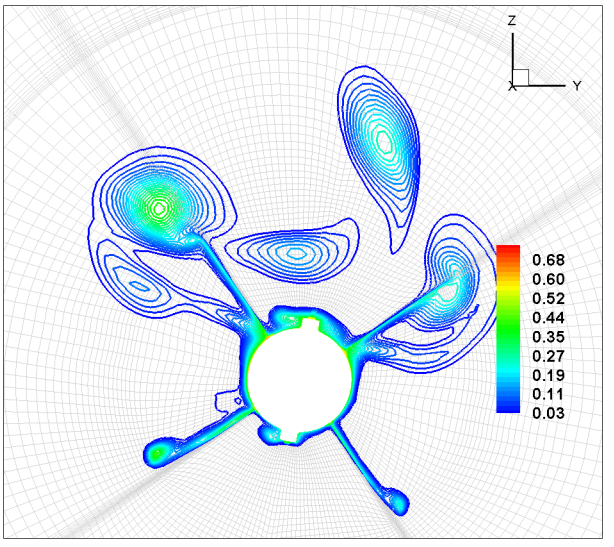

Fig. 23 Crossflow vortices at $X = 20.8D$.

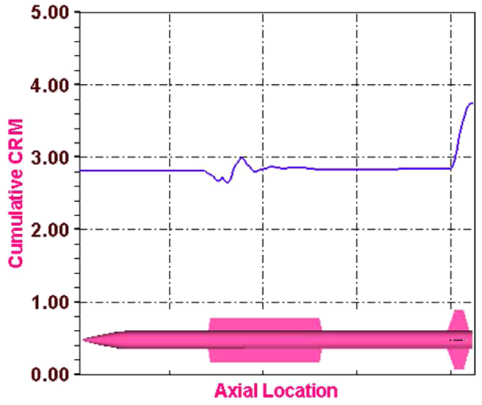

Fig. 24 Cumulative CRM distribution ($\phi = -34$ deg).

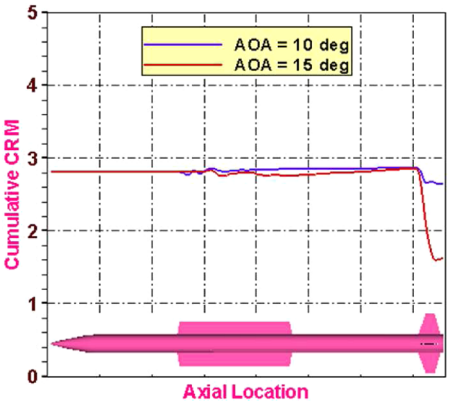

Fig. 27 Effect of AOA on cumulative CRM.

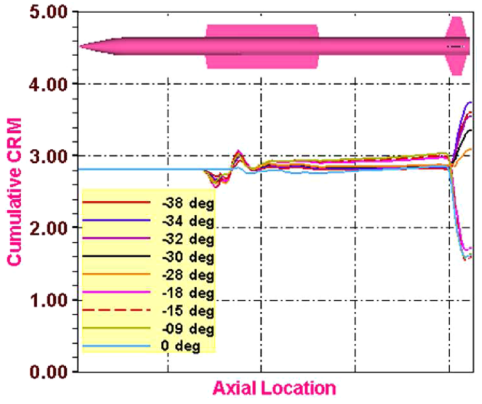

Fig. 25 Cumulative CRM distribution.

downstream of the wing starting location, the wire-tunnels start to contribute to the CRM and nullify the CRM due to the wing and produce a rolling moment opposite to that of the wing. The overall CRM due to the wing and wire-tunnel reaches a positive peak of about 3.0, and then begins to diminish further downstream, up to the termination of the wing. Further downstream, although the complexity of the flowfield increases, the rolling moment remains near 2.8. This continues up to the fin starting location and once over the fin, the sudden surge in CRM can be observed clearly, reaching a value of 3.8. The magnitude of the rolling moment was found to increase five-fold when integrated up to the fin, as compared with the rolling moment when integrated up to the wing region.

This picture clearly explains the cause of the severe rolling moments, in which the fins bear the brunt of the enormous surge in lateral loads. The cumulative CRM distributions for a few other roll orientations are presented in Fig. 25. Uniformly, the effect of CRM due to wing and wire-tunnel are opposite to each other for all the cases. The rolling moment value is almost insignificant, with a magnitude in the range of 2.8 (no rolling moment) to 3.0 (the fin starting location). Because of the physical phenomenon explained previously, the resultant lateral loads on the fins contribute to the large rolling moment , as can be seen from Fig. 25. A zoomed view of the cumulative CRM distribution around the fin zone is shown in Fig. 26. From the plot, it can be observed that there is a uniform and continuous increase in rolling moment over the fin beginning from the leading edges and accumulating large magnitudes till the trailing edges of the fins.

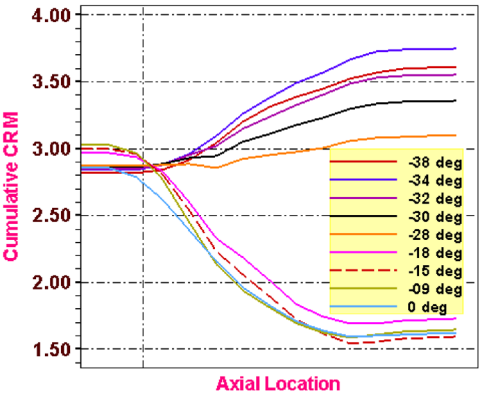

Fig. 26 Cumulative CRM distribution at fin.

F. Effect of Angle of Attack

It is interesting to note the effect of angle of attack on the rolling moment. Hence, a comparison is made between cumulative CRM plotted for Mach 1.2 at two angles of attack, viz., 10 and 15 deg at $\phi = 0$ deg.

Figure 27 shows the comparison, and it can be seen that at a 10 deg angle of attack, the cumulative rolling moment and hence the total CRM is almost equal to the null-rolling moment value and is about 2.6, whereas for a 15 deg angle of attack, the coefficient of rolling moment is about 1.6, which is about −1.2 away from the null-rolling moment value of 2.8. It implies that at an angle of attack of 10 deg, the flow is quite simple and uncomplicated due to the absence of complex vortical interactions on the missile itself. However, at an angle of attack of 15 deg, the flowfield tends to become highly complex due to vortical flow domination, creating large induced-roll. Thus, we can conclude that in the angle of attack range of about 10 to 15 deg, the nonlinear behavior on lateral characteristics starts to set in and the consequential high angle of attack phenomenon begins in this angle of attack range. It is the inherent configuration characteristics, which are governed by slenderness, wing/fin sizes, locations, and flow regimes, that dictate the flow phenomenon.

V. Conclusions

Lateral aerodynamic behavior of an air-to-air missile for critical flight conditions was characterized using 3D RANS code CERANS. The physical phenomenon that caused the severe induced roll during flight was explained. The asymmetric impingement of crossflow wing vortices on the fins had induced large lateral loads, leading to severe rolling moment of the missile. The need to study the rolling moment behavior at finer roll orientations was brought out.

Acknowledgments

The authors express their sincere gratitude to the Director, DRDL and Project Director, AAM for their constant support, tireless reviews, and encouragement. The support rendered by Scientists of Directorate of Aerodynamics is sincerely acknowledged.

References

[1] Balasubramanian, R., and Anandhanarayanan, K., "Indigenous Development of Compressible Reynolds Averaged Navier-Stokes Solver, CERANS," *DRDO Science Spectrum*, Defence Scientific Information and Documentation Centre (DESIDOC), Ministry of Defence, Defence Research and Development Organization (DRDO), New Delhi, 2009, pp. 219–226.

[2] Anandhanarayanan, K., and Balasubramanian, R., "A Multiblock Approach for Simulating Control Surface Deflections of a Hypersonic Vehicle," *Journal of Aerospace Quality and Reliability*, Vol. 1, No. 2, July 2005, pp. 61–66, India.